MASTER THESIS

International double degree Master's program

Nanotechnologies for the ICTs and Quantum Devices

Semiconductor Saturable Absorber Mirrors in the mid-IR

Candidate:
Raffaele Riccio

Academic supervisors:
Carlo Ricciardi, Maria Luisa Della Rocca

Internhsip supervisors:
Raffaele Colombelli, Mathieu Jeannin

Hosting institution:
C2N - Centre de Nanosciences et de Nanotechnologies

Academic year: 2022/2023

Contents

Acknowledgement

First and foremost, I would like to express my deepest gratitude to my supervisors Raffaele Colombelli and Mathieu Jeannin, not only for giving me the opportunity to be part of this project, but also for demonstrating unparalleled enthusiasm and insight towards scientific research. I would like to thank the entire team for welcoming me from day one and for showing themselves as not only highly knowledgeable scientists but also as wonderful individuals. In particular, I would like to thank my predecessor Eduardo Cosentino, for being the best mentor I could have asked for during these months.

I would like to express my gratitude to my adventurous companion, Andrea, who shared the joys and challenges of these 9 months in Paris with me. And from afar, a huge thank you to my friends Noemi, Gabriele, and Floriana, who have never ceased to make me feel their support in this adventure. I have always felt your presence with me.

Lastly, the greatest thanks go to those who made all of this possible: my parents, my sister, and my brother. Thank you for always believing in me far more than I have ever believed in myself.

Mid-IR/THz Quantum Devices Group - C2N Photonics Department

The Centre for Nanosciences and Nanotechnology (C2N) is a joint research unit between the CNRS and Université Paris-Saclay. The center develops research in the field of material science, nanophotonics, nanoelectronics, nanobiotechnologies and microsystems, as well as in nanotechnologies. In all these fields, the research activites span from fondamental to applied science. With a cleanroom of 2900 sqm, technological facilities are a central element in the research carried out in the laboratory, thanks to the presence of 40 expert engineers in the use of state-of-the-art equipment for micro and nano technologies. This intership has been carried out in the Mid-IR/THz team belonging to the Optoelectronic Devices and INovation (ODIN) group in the Photonics Department. The goal of the team is to develop new semiconductor-based optoelectronic devices in the still partially uncovered mid-IR portion of the electromagnetic spectrum. To do so, the group relies on a solid state approach based on optical transitions between the confined energy levels the conduction band of Quantum Wells (QW), the so-called intersubband transitions. These transitions are at the heart of various devices such as Quantum Cascade Lasers (QCL), Polaritonic light emitting diode (LED) and Quantum Well Infrared Photodetectors (QWIP). In addition, the team is experienced and actively engaged in the investigation of intersubband polaritons physics and its potential application in the development of novel devices, foremost among them SESAMs operating in the mid-IR, polaritonic lasers, and ultrafast modulators.

Chapter 1

Introduction

The mid-infrared (mid-IR) region of the electromagnetic spectrum, typically spanning wavelengths between 3 and 30 micrometers, has garnered increasing interest in recent years due to its unique properties and diverse range of applications. Unlike other spectral regions, many fundamental mid-IR optoelectroctonic devices rely on intersubband transitions, a phenomenon that occurs within quantum wells or quantum cascade structures, making it an intriguing and promising field of exploration. Optoelectronic devices operating in the mid-IR range offer numerous applications and advantages. One notable area is spectroscopy, where the mid-IR provides fundamental information about the vibrational and rotational modes of molecules. This enables precise chemical analysis, environmental monitoring, and gas sensing, with applications ranging from detecting pollutants to identifying biomarkers for medical diagnostics. Additionally, the mid-IR holds potential in the field of telecommunications thanks to the atmospheric transparency in its range of wavelengths. The mid-IR's reduced absorption and scattering by water molecules make it well-suited for biomedical applications, including non-invasive imaging, remote sensing, and detection of diseases.

1.1 Limitation and challenges in the mid-IR

Despite the promising prospects, the mid-IR range presents several challenges and limitations that have hindered the development of efficient optoelectronic devices. One of the primary challenges is the scarcity of versatile and high-performance optoelectronic devices tailored specifically for the mid-IR spectral region. While significant progress has been made in other parts of the electromagnetic spectrum, the mid-IR remains a relatively uncharted territory in terms of device development and integration. Our objective is to address some of these limitations and pioneer new solutions by focusing on the development of mid-IR polaritonic systems.. This endeavor is part of a broader effort to unlock the potential of the mid-IR range.

1.2 Operating principle of saturable absorber mirrors

Saturable absorption is a feature of many materials, in which the absorption depends on the intensity of the incident radiation:[18]

$$\alpha = \frac{\alpha_0}{1 + \frac{I}{I_{sat}}} \tag{1.1}$$

with α_0 the absorption at low incident intensity, and I_{sat} the saturation intensity at which the absorption is equal $\alpha = \frac{1}{2}\alpha_0$. An explicative scheme of the effect on reflectance is reported in Fig. 1.1: as the incident radiation intensity on the absorber increases, its reflectance grows until the saturation at

the unitary value. In the visible region of the spectrum, saturable absorbers have proven to be efficiently able to passively mode lock diode, color-center and solid-state lasers[3], gaining large success for their relatively low saturation fluence and low cost, leading to their exploitation in several applications.

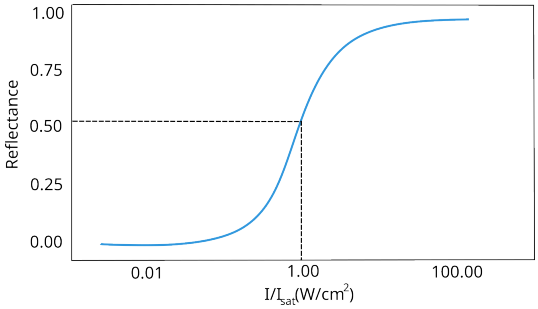

Figure 1.1: Characteristic non-linear reflectance of a saturable absorber: above I_{sat} the reflectance reaches 0.5 and then saturates to unity

This is possible thanks to the fact that the intensities needed to saturate the *interband* transitions on which these absorbers rely fit well the typical devices' output power in those spectral regions. On the contrary, the development of saturable absorber mirrors relying on *intersubband* transitions has been hindered, up to now, by the high intensities needed for the ISB transition saturation. These reach the order of several hundreds of kW/cm^2[1], which are incompatible with the average powers emitted by QCLs operating in the mid-IR. Although in recent years the upper limit has been pushed slightly above 3 μm thanks to the development of a SESAM based on InAS/GaSb type-II superlattice[19], SESAMs remain a missing piece in the toolbox of devices operating in this spectral region.

Chapter 2

Theory of intersubband cavity polaritons

2.1 Intersubband (ISB) transitions in semiconductor Quantum Wells

As mentioned, ISB transitions in quantum wells are an important tool for mid-IR optoelectronics. To understand how the transition mechanism works, we write down the Hamiltonian describing light and matter interacting:

$$H = \frac{(\vec{p} - q\vec{A})^2}{2m} + V_c(\vec{r}) + q\phi(r) \tag{2.1}$$

Where q and m are the electron charge and mass, $\vec{A}$ is the vector potential of the electromagnetic field, V_c is the crystal potential, and $\phi(r)$ is the electrostatic potential. Moving to the Coulomb Gauge : $\vec{\nabla} \cdot \vec{A} = 0,\ \phi(r) = 0$, we obtain that the operators associated with $\vec{p}$ and $\vec{A}$ commute. In the weak field limit, this leads to:

$$H = \frac{p^2}{2m} + V_c(\vec{r}) - \frac{q}{m}\vec{A} \cdot \vec{p} = H_0 + H_1 \tag{2.2}$$

With H_0 being the Hamiltonian of the unperturbed system, while $H_1 = -\frac{q}{m}\vec{A}\ \dot{}\vec{p}$ is the perturbing term due to the interaction with light. Considering now a harmonic oscillation of the field with amplitude E_0 and frequency ω

$$\vec{E}(\vec{r}, t) = E_0 cos(\vec{q} \cdot \vec{r} - \omega t)\hat{e} = -\frac{\partial \vec{A}}{\partial t} \tag{2.3}$$

this can be integrated to obtain the expression of the potential vector to insert in H_1

$$\vec{A} = \frac{E_0}{\omega} sin(\vec{q} \cdot \vec{r} - \omega t)\hat{e} \Rightarrow H_1 = \frac{qE_0}{m\omega}\hat{e} \cdot \vec{p}\ sin(\omega t) \tag{2.4}$$

Note that in the last step of (2.4) we eliminated the space dependence assuming that we are working in the electric dipole approximation, thanks to which we can consider the photon wavevector $\vec{q}$ negligible with respect to the electron momentum $\vec{k}$. This means that the k-vector of the electron is conserved in the interaction, standing for a vertical transition in momentum space. Now that we have derived the perturbing term of the Hamiltonian, we can treat the problem by means of the Fermi Golden Rule. According to the latter, one can write the transition rate between an initial $|i\rangle$ and a final $|f\rangle$ electronic

state in a quantum well as:

$$W_{if} = \frac{2\pi}{\hbar}|\langle f|\frac{qE_0}{m\omega}\hat{e}\cdot\vec{p}|i\rangle|^2\delta(E_f - E_i - \hbar\omega) \tag{2.5}$$

In our case, the states $|i\rangle, |f\rangle$ will belong to different subbands in the same conduction band of a quantum well's dispersion. We can now write the electronic state wavefunctions by using the envelope function approximation, and considering the envelope as product of a planewave in the tranverse plane (x, y), and a second function $\phi(z)$ arising from the confinement along the z direction. The envelope is multiplied by the Bloch periodic function. Starting from the most general case, each state will be characterized by three quantum numbers: the band the electron belongs to (α, β), the respective subband (n, m), and the in-plane wavevector:

$$\langle\vec{r}|n, \vec{k}, \alpha\rangle = u_{\alpha\vec{0}}\chi^{\alpha}_{n\vec{k}}(\vec{r}) = u_{\alpha\vec{0}}\frac{1}{\sqrt{S}}e^{i\vec{k}\cdot\vec{R}}\phi^{\alpha}_{n}(z) \tag{2.6}$$

Thus, we can write the states as $|i\rangle = |\alpha, n, \vec{k}\rangle,\ |f\rangle = |\beta, m, \vec{k'}\rangle$ and insert them in the perturbation matrix element of (2.5) to derive the requirements for the intersubband transition to occur:

$$\langle\beta, m, \vec{k'}|\hat{e}\cdot\vec{p}|\alpha, n, \vec{k}\rangle = \hat{e}\cdot\left[\int u^{*}_{\beta\vec{0}}u_{\alpha\vec{0}}(\chi^{\beta}_{m\vec{k'}})^{*}\vec{p}\chi^{\alpha}_{n\vec{k}}\cdot d\vec{r} + \int(\chi^{\beta}_{m\vec{k'}})^{*}\chi^{\alpha}_{n\vec{k}}u^{*}_{\beta\vec{0}}\vec{p}u_{\alpha\vec{0}}\cdot d\vec{r}\right] \tag{2.7}$$

Note that here the value of the two integrals is determined by the action of the momentum operator on the two different functions. The development of the second term on the right side of the above equation leads to the *interband* transition selection rule, so we won't consider it. On the contrary, looking at the first integral, one can consider the slow variation of the envelope function at the unit cell scale, thus writing everything in terms of a summation over each unit cell of a single cell integral. Note that, in this way, the envelopes can be considered constant over Ω_{cell} and thus can be taken out of the integral. Doing this, the expression reads

$$\sum_{i=1}^{N_{cell}}(\chi^{\beta}_{m\vec{k'}})|_{Ri}\vec{p}\chi^{\alpha}_{n\vec{k}}|_{Ri}\int_{\Omega_{cell}}u^{*}_{\beta\vec{0}}u_{\alpha\vec{0}}\cdot d\vec{r} \tag{2.8}$$

where the integral represents the scalar product of two orthogonal functions, as long as their indices are different. This means that the whole term is different from zero only if $\alpha = \beta$, i.e. if the transition occurs within the same band, from a subband to another. Further developing the term out of the integral one finds that, with $\alpha = \beta$, this is different from zero only when the two subbands involved in the transition, m and n, have opposite parity. This is known as the *parity selection rule*. Note that the latter holds only in the case of systems whose Hamiltonian commute with the parity operator. When this is not true, as in the case of asymmetric coupled quantum wells, the different parity transitions are no longer prohibited. We have defined a process in which, interacting with radiation, an electron is excited from a subband to a second one belonging to the same band. This process takes the name of *intersubband* transition and it is an exclusive feature of confined systems. The most immediate is the $1 \to 2$ transition in the conduction band of a quantum well. A sketch is depicted in Fig. 2.1. There is a last selection rule that is necessary to derive to understand the excitation mechanism of intersubband transitions. Let us consider what remains of (2.7), considering again only the first right handed integral term and setting the integral in (2.8) equal to 1. We still have

$$\langle\chi_{m\vec{k'}}|\hat{e}\cdot\vec{p}|\chi_{n\vec{k}}\rangle = \langle\chi_{m\vec{k'}}|e_xp_x|\chi_{n\vec{k}}\rangle + \langle\chi_{m\vec{k'}}|e_yp_y|\chi_{n\vec{k}}\rangle + \langle\chi_{m\vec{k'}}|e_zp_z|\chi_{n\vec{k}}\rangle \tag{2.9}$$

Here, the only non zero term is the last one:

$$\langle\chi_{m\vec{k'}}|e_zp_z|\chi_{n\vec{k}}\rangle = e_z\int e^{i(\vec{k}-\vec{k'})\cdot\vec{R}}\cdot d\vec{r}\int\phi^{*}_{m}p_z\phi_n = \delta_{\vec{k},\vec{k'}}\langle\phi_m|p_z|\phi_n\rangle \tag{2.10}$$

We have thus derived the *polarization selection rule* for intersubband transitions: they are allowed only by a radiation whose electric field is polarized in the direction of the quantum well's growth, z in this case.

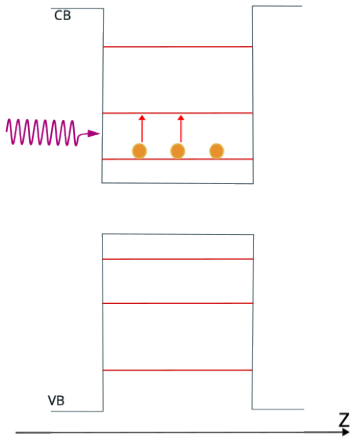

Figure 2.1: Sketch of the intersubband excitation in the band diagram of a quantum well

We can now introduce a last important quantity playing a role in the interaction between light and matter. According to the definition of the absorption coefficient as energy absorbed per unit time and volume over the intensity of the incident radiation, we can write it for the fundamental transition as $\alpha = E_{21} W_{21} \frac{n_s}{L_{QW}}$, where n_s is the surface electron density, L_{QW} is the length of the quantum well, and E_{21} is the energy of the transition. We have already derived the transition rate W_{21}, in which we now introduce a broadening factor accounting for the finite dephasing time of the electrons:

$$\delta(E_2 - E_1 - \hbar\omega) \rightarrow \frac{\gamma}{\pi(E_2 - E_1 - \hbar\omega)^2 + \gamma^2} \tag{2.11}$$

Finally, we can define the oscillator strength of the transition appearing in the expression of α as

$$f_{21} = \frac{2m^* E_{21}}{\hbar^2} | < \phi_2 | \hat{z} | \phi_1 > |^2 \tag{2.12}$$

standing for the efficiency of a given transition in its interaction with light. According to Thomas-Reiche-Kuhn sum rule, the summation of the oscillator strenghts over all the possible transitions is

$$\sum_m f_{mn} = 1 \tag{2.13}$$

However, considering the calculation for the $1 \rightarrow 2$ ISB transition for an infinite barrier quantum well of thickness L, one easily finds that $f_{21} \approx 0.96$, meaning that most of the oscillation is concentrated in the $1 \rightarrow 2$ transition, which is thus practically the only responsible of the intersubband absorption. Considering the practical case of a non-infinite barrier quantum well, the oscillator strength of a given ISB transition depends on the electron effective mass and on the penetration of the electronic wavefunctions in the potential barriers.

2.2 Properties of metal-insulator-metal microcavities

Microcavities constitute an important instrument of quantum photonics, being able to ”capture” the incident radiation and to confine it at sub-wavelenght scale. In metal-insulator-metal cavities, the reflective properties of the metal allow for sub-wavelength confinement between two metallic plates. The extent of

this confinement plays a crucial role in enabling a strong interaction between radiation and matter when the cavity is filled with an active medium.[5]. It is known in fact, that the light-matter coupling coefficient is inversely proportional to $\sqrt{V_0}$, where V_0 is the effective volume of the electromagnetic mode of the field. The typical optical response of a MIM microcavity can be observed by means of a reflectance spectrum, obtained by an incident radiation on the cavity itself. Looking at its dependence on the frequency, the reflectance spectrum will be characterized by dips, corresponding to the resonant condition between the electromagnetic field of the radiation and the cavity mode. For the purposes of this work, it is important to understand how the properties of these cavities depend on their geometrical characteristics. Considering an array of metal-insulator-metal microcavities, the three most influencing geometrical parameters are: the lateral size s of the single patch cavity (in our case we will deal with square shaped cavities), distance p between two adjacent cavities, and the thickness L of the cavities. When dealing with sub-wavelength thicknesses L, as in this entire work, the cavities are $non-dispersive$, meaning that the resonant frequency shows no dependence on the in-plane wavevector $k_{//}$, and thus on the incident angle[4]. However, by increasing the cavity thickness, the frequency bands tend to progressively lean on the fundamental mode TM_0 dispersion, giving thus dispersive cavities whose interactions with ISB systems have been studied in several works[13][20]. In this present case, we are mostly interested in the effects of the array's filling factor, and thus of p, on the interaction with the radiation. First thing, once a photon is injected into the strongly localized mode of a cavity, what will happen is determined by the competing dissipation mechanisms in the system. When the radiative and non radiative losses, γ_r and γ_{nr} respectively, are equal, the system is in the so called *critical coupling* condition. In this regime, which can be accessed by a proper control of p, all the energy fed to the system is dissipated in the system itself. Thus, the existence of critical coupling represents an important factor in the development of perfectly absorbing optoelectronic devices. In addition to be a crucial parameter in the behavior of confined photons inside the cavity[12], the distance between the patches has a strong influence on the way the light is collected by the resonator itself. It is known that microcavities display a photon collection area that is larger than the surface of the cavity itself, a phenomenon known as $funneling$.

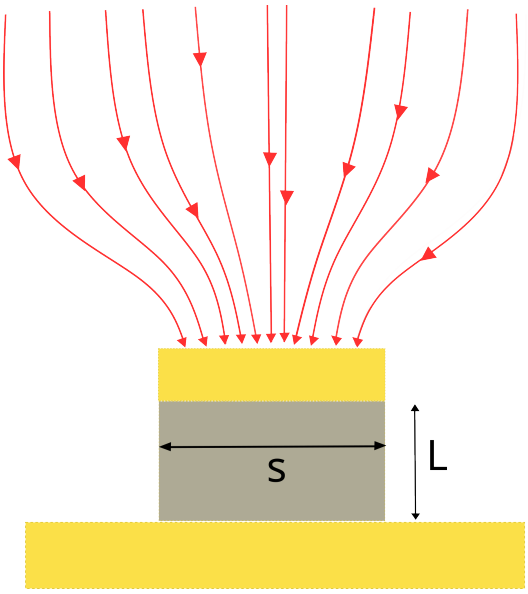

Figure 2.2: Sketch of the funneling mechanism in a metal-insulator-metal cavity: the field line outside the patch surface are bent to converge on it. Also, the thickness L and the lateral size s of the cavity are indicated

It has already been shown that this mechanism, which depends on the filling factor of the array, can be exploited to amplify the photon harvesting in nanometric devices, especially in the framework of photodection[15][11]. The mechanism can be explained in terms of a bending of the Poynting vector streamlines from the incident field, converging to the cavity because of a magneto-electric interference with the evanescent field from the metallic surface[7], as sketched in Fig. 2.2. It is important to note that in the case of reference[7] the study is conducted on sub-wavelength grooves on the metallic layer, and not MIM cavities.

2.3 The strong light-matter interaction: ISB polaritons

We have now all the elements to describe the interaction between the resonant mode of a cavity and a two-level system (Fig. 2.3). The interaction between the two sub-systems is resonant when their frequencies, ω_c of the cavity and ω_{21} of two-level system, coincide. When this happens, the entity of the interaction is determined by three parameters:

- γ_c: the cavity decay rate
- γ_{21}: the two-level system decay rate
- Ω_R: the coupling strength between the two sub-systems

when the coupling strength is larger than the system losses, i.e. when $\Omega_R > max(\gamma_{21}, \gamma_c)$, the system enters the so called *strong coupling* regime: the ligth interaction with the two-level system becomes a reversible process, with the photon undergoing several absorptions and emissions before leaving the cavity.

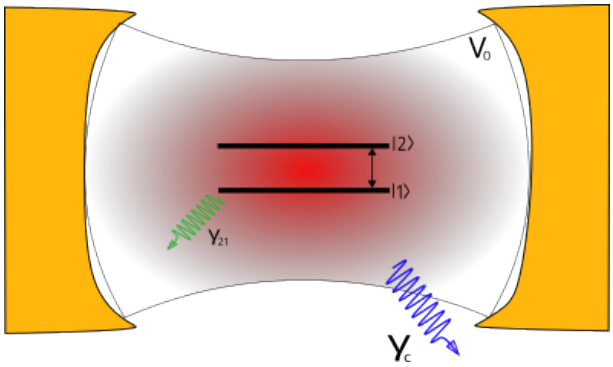

Figure 2.3: Scheme of light-matter interaction in the resonator: the strong coupling is achieved when the coupling strength Ω_R overcomes the two decay rates γ_c and γ_{21}

We can write the Hamiltonian of the two-level system and of a quantized radiation field as

$$H_{mat} = E_1|\Psi_{1,\vec{k}}\rangle\langle\Psi_{1,\vec{k}}| + E_2|\Psi_{2,\vec{k}}\rangle\langle\Psi_{2,\vec{k}}| \qquad H_{phot} = \hbar\omega_c(a^\dagger a + \frac{1}{2}) \tag{2.14}$$

where $E_{1,2}$, $|\Psi_{1,2,\vec{k}}\rangle$ are the upper ad lower energies and states, respectively, while a, $a^\dagger$ are the photon destruction and creation operators. Starting from $H_{int} = -\vec{d}\cdot\vec{E}$, where $\vec{d}$ is the electric dipole operator

and $\vec{E}$ is the electric field operator, we can include the interaction by writing the total Hamiltonian of the system in the rotating wave approximation:

$$H_{tot} = H_{mat} + H_{phot} + H_{int} = \begin{pmatrix} \hbar\omega_c & i\hbar\Omega_R \\ -i\hbar\Omega_R & \hbar\omega_{21} \end{pmatrix} \tag{2.15}$$

The result of the diagonalization are mixed light-matter states, called cavity *polaritons*, described as linear superposition of an electronic excitation and a cavity photon. In the case of interest of this work, the coupling constant Ω_R of the ISB transition is[16]

$$2\Omega_R = \sqrt{\frac{e^2 f_{21}}{\epsilon_0 \epsilon_r m^* V_0}} \tag{2.16}$$

with V_0 the effective volume of the mode in the resonator. We can finally write the eigenergies of the system, standing for the *upper polariton* and *lower polariton* energies, as function of the detuning $\Delta E = E_c - E_{21}$.

$$E_{UP,LP} = \frac{1}{2}(E_{21} + E_c \pm \sqrt{\Delta E^2 + (2\hbar\Omega_R)^2}) \tag{2.17}$$

The resulting dispersion is reported in Fig.2.4: for high detuning, the two polariton branches follow asimptotically E_{21} and E_{cav}, as if the system is not in strong interaction. When the zero detuning is approached, the branches are bent, resulting in an $anti-crossing$ pattern, characteristic of the strong coupling regime, with the splitting in the point of minimum distance equal to $2\hbar\Omega_R$

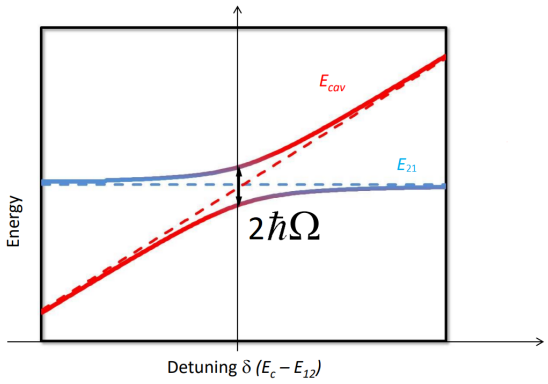

Figure 2.4: Anticrossing dispersion characteristic of the strong ligth-matter coupling: as we get close to the resonant condition between the cavity and the two-level system, the energy curves of the two separated systems are bent forming a point of minimum splitting $2\hbar\Omega_R$

It's now time to substitute the general two-level system with the several intersubband transitions occurring in a semiconductor quantum well. The result of the strong coupling between the collective excitation of the intersubband transition in a 2D electron gas - the ISB plasmons - and light is a mixed state called *intersubband polariton*[2][9]. It can be demonstrated that, when inserting a QW with surface electron density n_{2D} and N ISB transition resonantly coupled with the cavity mode $E_{21} = E_c$, the Jaynes-Cumming model leads to

$$2\Omega_R = \sqrt{\frac{e^2 f_{21} n_{2D}}{\epsilon_0 \epsilon_r m^* L_{QW}}} \sqrt{\Gamma_{opt} f_w} \tag{2.18}$$

where L_{QW} is the quantum well width and the first square root constitutes the plasma frequency of the 2D electronic system

$$\omega_p = \sqrt{\frac{e^2 f_{21} n_{2D}}{\epsilon_0 \epsilon_r m^* L_{QW}}} \tag{2.19}$$

Γ_{opt} is the *optical mode confinement factor* and takes into account the overlap between the spatial distribution of the resonator mode and the active region containing the QWs:

$$\Gamma_{opt} = \frac{\int_{AR} |E_{k,z}|^2 \, dz}{\int |E_k|^2 \epsilon(z) \, dz} \epsilon_{AR} \tag{2.20}$$

with ϵ_{AR} the dielectric constant of the active region material. f_w, instead, is the *quantum well overlap factor* accounting for the percentage of active region that is covered by the QWs, and can be written as

$$f_w = \frac{L_{eff}}{L_b + L_w} \tag{2.21}$$

where L_b, L_w are respectively the width of the barrier and of the well, while L_{eff} is the effective width of the quantum well accounting for the spatial extension of the electronic wavefunction.

Chapter 3

Coupled Mode Theory (CMT) for the ISB absorption saturation

Before moving to the experimental results, we will briefly introduce the study of intersubband absorption saturation in the strong ligth-matter regime. By approaching the problem by means of temporal Coupled Mode Theory (TCMT), we'll be able to derive a set of analytical equations describing the saturation mechanism and the triggering of non-linear reflectivity.

3.1 Coupled Mode Theory

Coupled Mode Theory is based on the modelization of the system under analysis as a closed system in which *oscillators* (such as the electronic collective oscillations or the modes of the EM field) are coupled to the external world through ports. Thus, we can describe both the ISB transition and the cavity mode using (ω_i, γ_i, Γ_i), which respectively stand for the natural oscillation frequency, the non radiative and radiative damping rates of the two interacting systems. When in presence of an external excitation, the system's response is described by the equations:

$$\frac{da_{isb}}{dt} = (i\omega_{isb} - \gamma_{isb})a_{isb} + i\Omega_R a_c \tag{3.1}$$

$$\frac{da_c}{dt} = (i\omega_c - \gamma_n r - \Gamma_r)a_c + i\Omega_R a_{isb} + \sqrt{2\Gamma_r}s^+ \tag{3.2}$$

$$s^- = -s^+ + \sqrt{2\Gamma_r}a_c \tag{3.3}$$

$$n_2 = 2\tau_{21}\gamma_{isb}\frac{|a_{isb}|^2}{N_{qw}\hbar\omega} \tag{3.4}$$

where a_i, γ_i are respectively the oscillation amplitude and the non radiative damping rate referring to the ISB transition and the cavity, Γ_r is the radiative decay rate of the cavity, τ_{21} is the lifetime of the higher energy state, s^+ and s^- are the amplitudes of the incoming and reflected fields. Placing ourselves in the case of harmonic fields of the form $s^+ = e^{i\omega t}$, we can solve the system and compute the intersubband absorption when the cavity and the ISB transition are at resonance ($\omega_{isb} = \omega_c = \omega_0$):

$$A^{ISB} = \frac{4\omega_{isb}\Gamma_r\Omega_R^2}{(\gamma_{isb}(\gamma_{nr} + \Gamma_r) - ((\omega - \omega_0)^2 - \Omega_R^2))^2 + (\gamma_{isb} + \gamma_{nr} + \Gamma_r)^2(\omega - \omega_0)^2} \tag{3.5}$$

we can now plug (3.5) in the expression of the surface density of electrons n_2 excited to the high energy subband:

$$n_2 = \frac{I}{N_{qw}\hbar\omega}\tau_{21}A^{ISB}(\Delta n, \omega) \tag{3.6}$$

according to this, we define the saturation intensity as the value of the intensity such that $n_2 = \frac{n_s}{4}$:

$$\frac{n_s}{4} = \frac{I_{sat}}{N_{qw}\hbar\omega}\tau_{21}A^{ISB}(\frac{n_s}{2}, \omega) \tag{3.7}$$

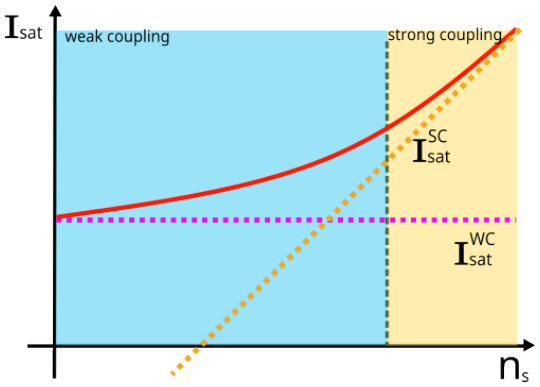

Figure 3.1: Scheme of the I_{sat} dependance on the surface doping density n_s. The dashed lines indicate the weak coupling (purple) and strong coupling (orange) saturation intensities. While the former is independent on n_s, the latter increases linearly.

It is found that the resulting behavior for the saturation intensity in weak and strong coupling regime differs in the dependance of I_{sat} on the doping. While in weak coupling I_{sat} does not depend on n_s, the saturation intensity in strong coupling regime increases linearly with the doping, as reported in Fig. 3.1. By developing the expression of I_{sat} in the weak coupling regime, we can access its relationship with the saturation intensity in a cavity-free system:

$$I_{sat}^{WC} = f_{21}\frac{\pi L_{AR}}{(\lambda/n_{opt})}\frac{Q_r}{2Q_{cav}^{tot^2}}I_{sat}^0 \tag{3.8}$$

with f_{21} being the oscillator strenght of the ISB transition, L_{AR} the total thickness of the active region and Q_r and Q_{tot} the radiative and total Q-factor of the cavity. Formula (3.8) expresses the possibility to decrease the saturation intensity of the insterubband transition thanks to the presence of a cavity. First, the linear dependance on L_{AR} tells us that we can reduce the saturation intensity by squeezing the field in ultra-subwavelength volumes. Secondly, we can optimize the branching ratio of the cavity quality factors. This will require the minimization of material losses (ensuring a large Q_{nr}) while remaining within the critical coupling condition $Q_{nr} = Q_r$ which allows us to maximize the energy feeding into the system. In addition to reducing the saturation intensity, the key requirement for developing a saturable absorber mirror is to achieve a significant variation in the optical response, resulting in an increased reflectivity. For this reason, a relevant limitation is observed for systems operating in the weak coupling regime as described by (3.8). The low-intensity saturation requires in fact to keep an elevated value of the overlap factor f_w. In the mid-IR, this is possible only using MIM cavities. In these type of resonators the losses are dominated by ohmic dissipation in the metals, making impossible to operate in the weak coupling regime, since the spectral reflectivity would be almost unchanged passing from non-saturated to saturated condition.

3.2 ISB saturable absorber mirror: collapse of the strong coupling and reflectivity increase

In the previous section, we justified why the weak coupling regime is not suitable for the development of the mid-IR SESAM: we want a system that needs a small intensity to exhibit a large variation of reflectivity.

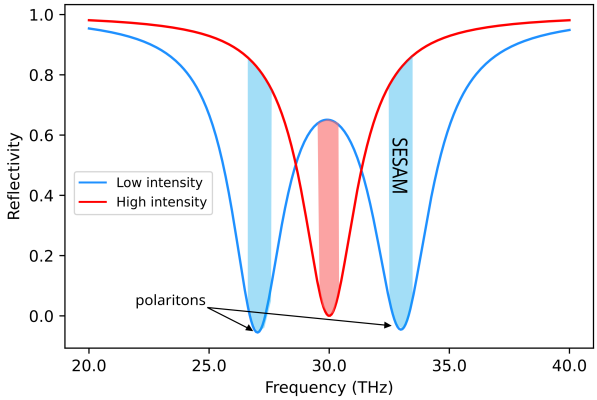

Figure 3.2: Collapse of the light-matter coupling: placing ourselves on the polariton resonances, the increase of the intensity causes an increase of the reflectivity as the two polaritons collapse

To do this, we need to place ourselves at the onset of the strong coupling regime. Here, at low intensity, ISB - cavity polaritons determine the presence of two minima in the reflectance spectrum. Approaching the saturation intensity, the ISB transitions become saturated, and we observe the collapse of light-matter interaction, with only the presence of the cavity resonance (Fig. 3.2). Looking at the two polariton features in the spectrum, the saturation causes a substantial increase of the reflectivity: this can be exploited as driving mechanism of the saturable absorber mirror. At low intensity, the presence of the polariton leads to a decrease in reflectivity, as the incident radiation is predominantly absorbed by the active region. Once the intensity overcomes I_{sat}, the lower energy subband is emptied and the strong coupling collapses determining the reflectance increase[10]. Note that to obtain a significant variation of the reflectivity it is important to ensure a sufficiently high contrast of the polariton spectrum. Therefore, the critical coupling condition will play a crucial role also in the case of strong light-matter coupling[14]. The critical coupling condition also has a significant impact on the saturation intensity. Being close to the critical coupling results in a higher efficiency of photon injection, thereby reducing the required intensity for achieving absorption saturation.

Chapter 4

Experimental results

In this chapter, the experimental set-up and the results that have been obtained will be presented and discussed. An introductory description of the different samples will be followed by three results: first, the low intensity reflectance spectra both of the doped and undoped samples, obtained by means of Fourier transform infrared (FTIR) spectroscopy. Then, we will describe a second set-up, allowing us to study the absorption saturation by means of a higher incident intensity using a QCL. We will then go through a fine measurement of the laser focus spot size by means of knife-edge method. This allowed us to determine the actual value of the incident intensity. Finally, we will conclude discussing the saturation response of the microcavity array as a function of the filling factor ff.

4.1 Samples structure and fabrication process

Despite the fact that I did not take part directly in the fabrication of the samples described in the following, it is worth to mention the fundamental steps involved in the process. All the samples that have been studied are made of metal-semiconductor-metal square microcavity arrays. The semiconductor region is constituted by a repetition of seven GaAs/AlGaAs quantum wells stacked between upper and lower layers of gold. The structures are realized by gold thermo-compressive wafer bonding of the GaAs wafer, with active region and gold layer deposited on its surface, to a second host layer of GaAs. After the bonding, the growth substrate is selectively removed using mechanical polishing, chemical etching in a citric acid solution and a final etch step using HF. Finally, electron beam lithography and lift-off steps, following the upper gold layer deposition, allow to obtain the structure sketched in Fig. 4.1.

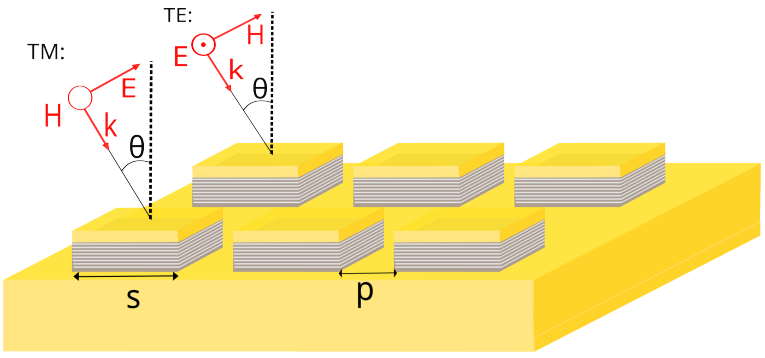

Figure 4.1: Representation of the sample structure: the QWs are embedded in square Au patches of size s with a continuous ground plane. They are separated by the distance p one from the other.

Here, the geometrical parameter s indicates the lateral size of a single patch, while p indicates the pitch, i.e. the distance between two consecutive patches. Each sample contains several arrays like the one in Fig. 4.1, each characterized by different s and p. In the following sections, three different samples will be analyzed and discussed: HM4445, a reference undoped sample with pitch size equal to 1μm; HM4447, identical to HM4445 but with delta-doping leading to a nominal surface density of 2 10^{11} cm^{-2}; HM4448-A-2, with the same nominal doping of HM4447, but presenting a larger number of different pitches p.

	Doping density (cm^{-2})	pitch p (μm)
HM4445	/	1
HM4447	2 10^{11}	1
HM4448-A-2	2 10^{11}	1-10

Table 4.1: The three samples under study, the respective doping density and pitch size.

4.2 Low intensity measurements

The first measurement performed is a low intensity Fourier transform infrared (FTIR) spectroscopy of both the undoped and doped samples. In FTIR, the globar optical response of the system is observed by measuring the intensity of the IR light reflected from its surface. The result of the measurement is a continuous broadband distribution of intensities as function of the frequency, containing important information on the energy levels in the sample. A scheme of the FTIR basic principle is reported in Fig. 4.2. A light source emits a broad range of wavelengths in the mid-IR region toward a beam splitter, generating a sample and a reference beams. The two beams are reflected back by a fixed and a movable mirrors. Thanks to the beam splitter, the reflected beams are recombined and directed to the sample. The reflectance signal from the sample is finally recorded by a detector.

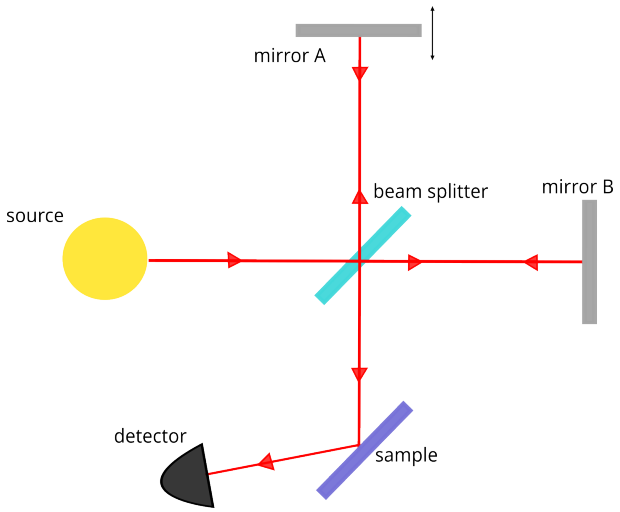

Figure 4.2: Scheme of FTIR spectroscopy: reaching the beam splitter, the original beam is divided in two beams toward a movable mirror A and a fixed mirror B. Once reflected, the two are recombined together after the beam splitter. A detector record the signal reflected from the sample while the movable mirror is displaced at constant velocity.

As the movable mirror position is displaced at a constant velocity, the detector will record an alternation of intensity maxima and minima, due to the constructive and destructive interference between the two beams. The final result, once the mirror has stopped moving, is the interferogram of the sample as a function of the mirror displacement. Then, the system performs the Fourier Transform of the latter, converting the interferogram from the space to the spatial frequency domain, and thus allowing us to access the sample reflectance at different wavelengths. In our case the analysis is performed using a Spectrometre IR-TF Nicolet. The instrument implements a mid-IR light source, covering the wavelength range of 600 - 6500 cm^{-1}, whose signal is focused on the sample through a microscope objective having numerical aperture NA=15 and x15 magnification. Before the reflection, the beam is divided in two thanks to the presence of a KBr beam splitter. The final signal is recorder by a MCT detector, cooled down to 78K using liquid N_2 and averaging 50 scans before giving the final spectrum with resolution of 4 cm^{-1}. Before collecting the sample's spectrum, the reflectance signal from a gold surface is taken and used as reference. In this way, dividing the sample's signal by the latter we obtain a normalized reflectance spectrum, thus minimizing noise and every sort of interferring signal, such the spectral dips due to absorption of molecules in the atmosphere.

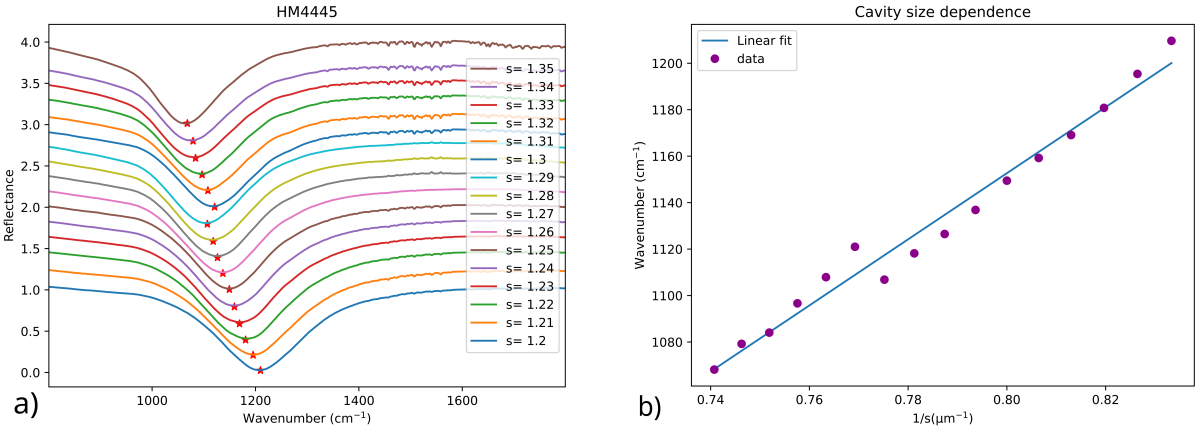

Figure 4.3: a) FTIR reflectance spectra of the undoped sample HM4445 for patches having different lateral size s. The red symbols indicate the position of the reflectance minima and so of the resonant frequencies. b) Data (purple, dots) and linear fitting (blue, continuous) of the spectral minima as function of $1/s$.

The FTIR reflectance spectra of undoped HM4445 and HM4447 are acquired as explained above and are showed in Fig. 4.3 and Fig. 4.4. For both samples, the spectra are measured for lateral size s ranging from 1.20 μm to 1.35 μm. From curve to curve, a vertical offset is introduced so to make the graph easier to read. In the case of HM4445, the curves have been fitted using a Lorentzian function and a unitary baseline:

$$R = 1 - \frac{A\sigma}{\pi[(x-\mu)^2 + \sigma^2]} \tag{4.1}$$

The reflectance minima corresponding to the cavity's resonant frequencies are well distinguishable (red symbols). In Fig. 4.3(b), we reported the dependence of the bare cavity resonant frequency on the inverse of the patch lateral size $1/s$. The data (purple dots) show an almost monotonically increasing behavior, with a single point of discrepancy that we attributed to some process imperfection in the electron beam lithography. The points are fitted using the linear dependence of the cavity frequency expressed by[6]:

$$w_k = \frac{K}{2n_M}\frac{1}{s} \tag{4.2}$$

Where K is the resonant mode order, s is the patch lateral size, and n_M is the effective modal index of the cavity. Note that, with respect to the reference, our frequencies are expressed in terms of wavenumbers in cm^{-1}, so a factor c is already simplified in our equation. Moreover, being the fundamental mode TM_0 the only one sustained in subwavelength cavities, with no cutoff frequency, we can consider $K = 1$. Eventually, we can extract the effective modal index from the fitted curve, which is found to be $n_M = 3.5$. The fact that the latter is larger than the bulk index of GaAs ($\mathrm{n}_{GaAs} \approx 3.3$) comes from the presence of an impedance mismatch at the interface between the metal-metal and single metal regions, thus allowing to confine light. The mechanism can be strongly influenced by changing the distance p between consecutive patches: the closer the cavities are, the easier is for them to *couple*, establishing a kind of cross-talking regime in which the field is no longer strictly localized in the single patch. We can now move to the analysis of the sample HM4447. Here, thanks to the doping, we expect the presence of electrons in the conduction band to activate the intersubband transitions, and thus in strong coupling, the ISB polaritons. For HM4447, in Fig. 4.4(a), the presence of both the cavity and the ISB transition in the quantum wells is reflected in a double reflectance minima in the spectrum.

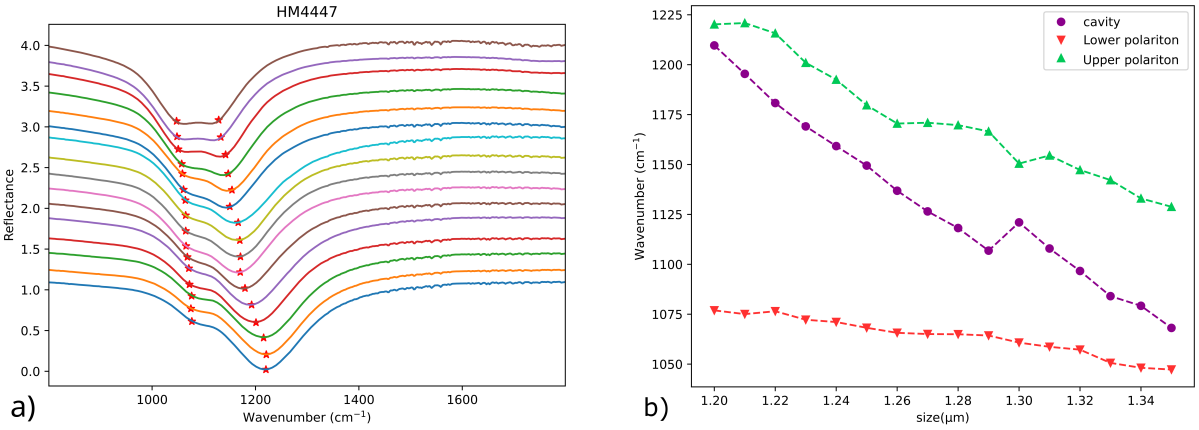

Figure 4.4: a) FTIR reflectance spectra for doped sample HM4447. The presence of ISB tranistion generates now the presence of two minima for each spectrum. b) Position of the upper polariton (green), lower polariton (red), and cavity's (purple) frequencies as a function of p

We can already point out that, in the presence of doping, the decrease of the lateral size s causes the distance and the unbalance in the contrast between the two dips to increase. This, as it will be showed in the following, corresponds to a departure from the point of minimum splitting in the anticrossing light-matter dispersion. As for the undoped case, the spectral curves are fitted with a double Lorentzian dip subtracted by a unitary baseline, according to the equation:

$$R = 1 - \frac{A\sigma_1}{\pi(x-\mu_1)^2 + \sigma_1} - \frac{A\sigma_2}{\pi(x-\mu_2)^2 + \sigma_2} \tag{4.3}$$

Again, from this we can extract the actual position of the minima as function of the patch size s. The result, together with the cavity frequencies, is reported in Fig. 4.4(b). We can finally use it to calculate the polaritonic dispersion as function of the bare cavity frequency.

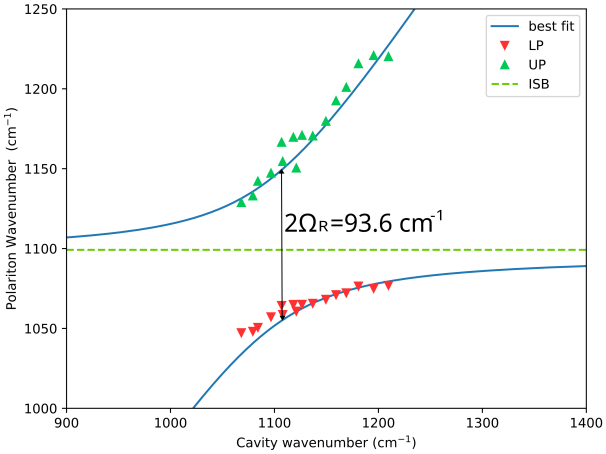

Figure 4.5: Intersubband polariton dispersion: the wavenumbers of the upper and lower polaritons are reported as function of the cavity's one. In this way, the anti-crossing dispersion characteristic of the strong light-matter interaction is observed. The data are fitted by means of the secular equation (blue), and the ISB transition wavenumber is reported (dashed green)

By doing it, as in Fig. 4.5, one can observe the characteristic anti-crossing behavior, thus witnessing the presence of strong light-matter coupling: the two polariton branches follow asymptotically the dispersions of the bare cavity and of the intersubband transition, but are bent around their intercept forming a region of minimum distance whose magnitude constitute the minimum Rabi splitting. The data points standing for the two polaritonic branches are fitted using the secular equation [8]:

$$(\omega^2 - \tilde{\omega}_{ISB}^2)(\omega^2 - \omega_c^2) = 4\Omega_R^2\omega_c^2 = \omega_P^2\ \omega_c^2 \tag{4.4}$$

where ω_c is the cavity frequency, Ω_R is the Rabi frequency, and $\tilde{\omega}_{ISB}$ is the intersubband transition frequency. Here, the *depolarization shift* coming from the collective oscillation of electrons is taken into account introducing the plasma frequency of the ISB system as

$$\tilde{\omega}_{ISB} = \sqrt{\omega_{ISB}^2 + \omega_P^2} \tag{4.5}$$

We thus have the possibility to extract the Rabi frequency, as being one of the fitting parameters of our curve. This is found to be Ω_R=46.8 cm^{-1}, meaning that the magnitude of the splitting between the two curves in terms of energy is about 11.6 meV. It is important to outline the value of the ratio $\frac{\Omega_R}{\gamma_{c,isb}^{tot}}$=0.36, where the denominator represents the total losses of the whole cavity/ISB system, obtained as full width at half maximum (FWHM) of the polariton reflectance dip. The fact that the Rabi frequency of the system is smaller but comparable with the losses ensures that we are at the onset of the strong light-matter regime. We can now use the expression of the Rabi frequency to obtain an experimental value for the doping in the active region of the sample

$$\omega_P = 2\Omega_R = \sqrt{\frac{f_{21}e^2 N_{QW}(N_1 - N_2)}{\epsilon\epsilon_0 m^* L_{cav}}} \tag{4.6}$$

Placing ourselves in the limit of very low excitation intensity - which is the case of FTIR - we can approximate the population difference between the first and second subband with the value of the doping

density $\Delta n = N_1 - N_2 \approx n$. In this way, we can invert the formula to find the doping

$$n = \frac{4\Omega_R^2 \epsilon \epsilon_0 m^* L_{cav}}{f_{12} e^2 N_{QW}} \approx 6.1\ 10^{10}\ cm^{-2} \tag{4.7}$$

by using $\epsilon = 12.88$, L_{cav}=192 nm, $m^* = 0.67 m_0$, $f_{21} = 0.96$, $N_{QW} = 7$
Note that the experimental value we found is substantially smaller than the nominal doping. Before moving to the second part of the experiment, we can already discuss a first effect of increasing p on the sample's response. To do that, we report the FTIR spectra obtained from sample HM4448-A-2 for different values of the pitch (Fig. 4.6(a)). For each p, the value of s is chosen so to find ourselves the closest possible to the anticrossing point. In this way, we are able to observe two almost symmetric polaritonic spectral features within the range of wavelengths covered by the chip 2 of the Quantum Cascade Laser that will be introduced in the second part of the experiment. The reflectance spectra were again fitted with two Lorentzian dips: an important information is contained in the contrast C of the polariton reflectance minima, indicating the balance between the incident photons and the portion absorbed feeding the ISB polaritons. The condition $C = 1$ corresponds to the so called *critical coupling* condition, in which all the incident power is effectively injected into the system. We defined the contrast as

$$C = 1 - R_{min} = A \tag{4.8}$$

- with A the system's absorption - and we calculated it for each reflectance minima FTIR spectra. The result is reported in Fig. 4.6(b): as the distance between the patches increases, the portion of the total intensity that is injected into the system gets progressively smaller.

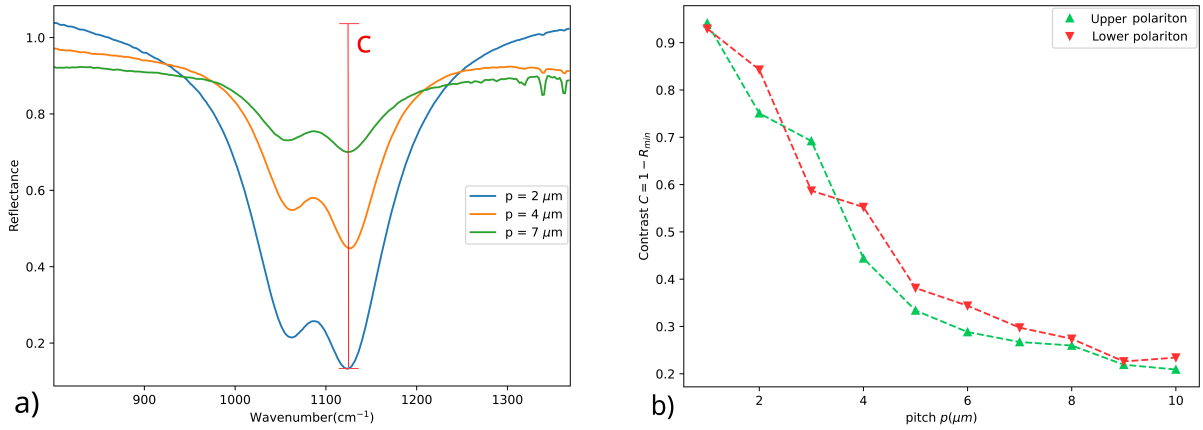

Figure 4.6: a) FTIR reflectance spectra for three different values of p in HM4448-A-2: it is already observable that the contrast in the spectrum diminishes as we increase the pitch. b) Plot of the contrast C as a function of p, with the latter ranging from 1 μ m to 10 μm

Finally, for completeness, we also report in Fig. 4.7 the polariton dispersion of sample HM4448-A-2. In this case, the frequencies of the polaritons (orange) and of the undoped's sample cavities (purple) are plotted as a function of lateral size. Thanks to the fact that sample HM4448-A-2 disposes of a wider range of s , we are now able to fully observe the transition through the anticrossing point. Again, polariton branches are fitted using the secular equation (4.4), while the linear fit of the cavities' frequencies is obtained using (4.2).

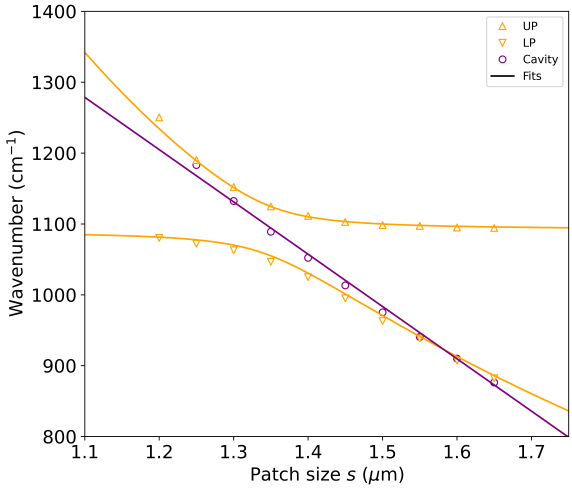

Figure 4.7: Anticrossing dispersion relation obtained from HM4448-A-2. The triangles represent the resonant frequencies of the upper and lower polaritons, reported as function of the lateral size and fitted using the secular equation (continous line, orange). As we get far from the anticrossing point, the dispersion follows the cavity (purple) and the intersubband transition lines

4.3 High intensity setup

In the following, the experimental set-up and procedures to study the behavior of the saturable absorbers under the incidence of a high intensity radiation will be discussed. The signal is coming from a commercial tunable QCL (Daylight MIRCAT), working with two chips to cover the range of wavelengths 1016 cm^{-1} - 1140 cm^{-1} for the chip 2, and 1140 cm^{-1} - 1320 cm^{-1} for the chip 1. The two chips display two different maximum operating currents: 850 mA (chip 1) and 1000 mA (chip 2). The laser is operating in pulsed-wave mode at a frequency of 50 kHz and pulse width of 100 ns, thus at a duty cycle of 0.5%. The beam is focused on the sample with a ZnSe objective with focal length of 18 mm, whereas the alignment is possible by checking first the microcavity array position illuminating the sample with a white light source and observing the reflected image using a visible camera. Once aligned, the mid-IR focus is adjusted by observing the reflected laser signal with a MIR microbolometric camera. The incident intensity on the sample can be tuned effectively in two ways: changing the current in the QCL at a given wavelength, up to a maximum of 1000 mA, and by means of an optical block made by a BaF_2 polarizer in series to a rotating half-wave plate. The rotation of the half-wave plate is finely controlled at single degree scale using a mechanical attuator. By keeping the polarizer at a fixed orientation, we obtain a transmitted intensity through this double element block that varies sinusoidally with the half-wave plate angle (Fig. 4.8(b)). In this way, we can easily tune the incident intensity between a minimum power condition, setting the transmittance of the $\frac{\lambda}{2}$plate - polarizer system to its minimum and driving the QCL at 600 mA - the onset of a stable lasing condition -, and a maximum power condition, removing the intensity modulator block and setting the current to the maximum value of 1000 mA. The signal is measured by a Mercury Cadmium Telluride (MCT) detector cooled down at low temperature using liquid N_2. A scheme of the complete setup is reported in Fig. 4.8(a)

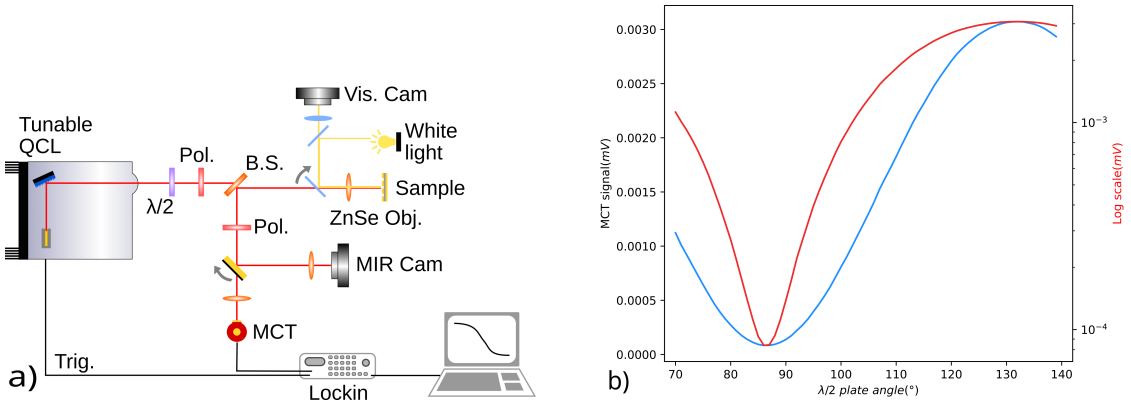

Figure 4.8: a)Scheme of the tunable intensity set-up: from the QCL, the signal is passed first through the optical block made of a half-wave plate and a BaF_2 polarizer in series that allow us control the intenity impinging on the sample. After, the beam is transmitted through a 90:10 beam splitter and focused on the sample by a ZnSe objective. The reflected signal is reflected by the beam splitter toward a second polarizer. This allows to attenuate the signal before getting measured. Finally, the direction of the beam can be easily switched between the MIR camera and the MCT. b)Calibration curve of the $\frac{\lambda}{2}$ plate+polarizer optical element both in linear (blue) and logaritmic (red) scale. Controlling the mutual orientation of the two optical elements we modulate sinusoidally the signal recorded. Here, the calibration is performed measuring the sample reflectance on the MCT.

The optical response of the sample is measured in reflection: the reflected signal is collected and directed by a series of mirrors that make possible to switch easily between the MIR camera and the MCT. A polarizer was placed in front of both of them to attenuate the intenisty of the reflected signal avoiding damaging the instruments.

4.4 Knife-Edge measurement of the laser focus spot size

To properly measure the absorption saturation and the nonlinear variation of the reflectivity as a function of the intensity, we needed to precisely determine the area of the incident laser spot on the sample. A laser beam is characterized by a Gaussian distribution of the intensity, being the Gaussian beam the fundamental solution of the electromagnetic field in the laser resonator. For a beam propagating in the z direction, the intensity distribution in the plane transverse to the propagation follows the equation

$$I = I_0 exp(\frac{-2(x^2+y^2)}{w^2}) \tag{4.9}$$

where I_0 is the maximum intensity amplitude and w is the beam radius, defined as the distance from the center of the beam at which the intensity is attenuated by a factor $1/e^2$. During the Gaussian beam propagation, the beam radius is not constant, but it increases diverging from a point of minimum magnitude, defined as waist w_0 (Fig. 4.9(a)).

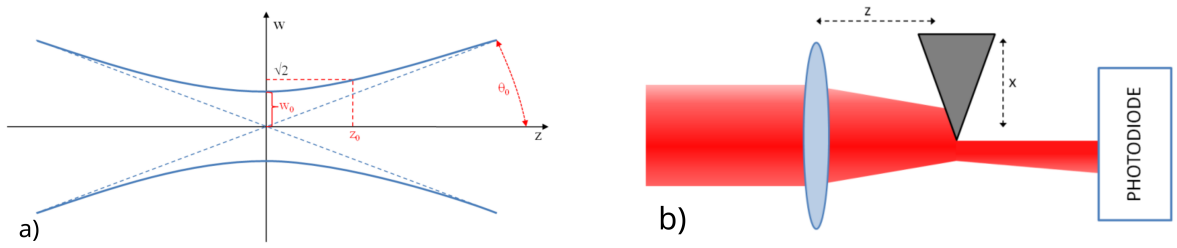

Figure 4.9: a) Gaussian beam propagation: the beam radius diverges as we get more distant from the waist point. b) Sketch of the knife-edge measurement: as the incident power is recorder by the powermeter, the knife blade is progressively moved in front of it until the whole beam is covered and the measured signal drops to its minimum.

When the laser beam is focused with an objective lens, the waist position after the objective lies at its focal length. A measurement of the focus spot size is necessary if we want to know precisely the incident area and thus the intensity of the radiation. A knife-edge measurement of this quantity consists in recording the power of the laser beam, while progressively covering the the beam using a knife blade placed at the focal distance from the objective lens and capable of moving in the plane perpendicular to the beam propagation. A sketch is given in Fig. 4.9(b). Moving the blade in front of the powermeter step by step, the read out signal progressively decreases until reaching its minimum when the beam is completely blocked by the knife. We can write down the power P recorded by the powermeter as[17]

$$P = P_0 \int_{-\infty}^{+\infty} dy \int_{-\infty}^{0} I(x + x_0, y)\, dx \tag{4.10}$$

Where I is the beam intensity, x_0 is the beam central position, and P_0 is a proportionality coefficient. In knife-edge method, the derivative $\frac{\partial P}{\partial x_0}$ of the power with respect to the beam position gives the beam intensity distribution (in the x direction) at the position $z = 0$ along the beam path. Note that the same distribution can be obtained in y changing the scanning direction of the blade. From the intensity distribution we can immediately access to the $1/e^2$ radius for a given z, and thus, varying the latter from a measurement to the other, we are able to reconstruct the Gaussian beam profile in Fig. 4.9(a) and finally determine the beam waist w_0.

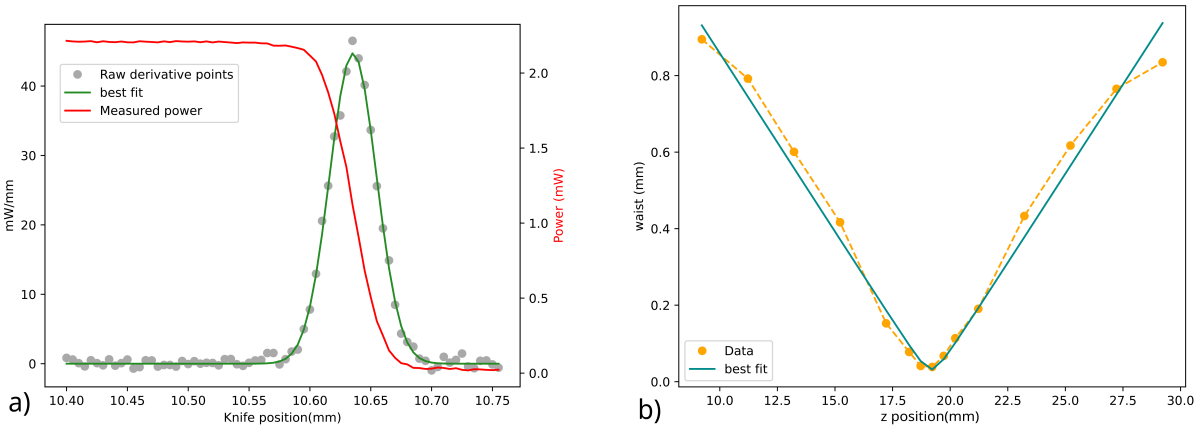

Figure 4.10: a) Red: power recorded by the powermeter as a function of the knife blade position in the x direction. Gray: Derivative of the measured power with respect to the blade position and (green) Gaussian fitting curve. b) Yellow: value of the $1/e^2$ radius obtained for each value of the knife position along the beam propagation direction z. Blue: fitting curve obtained using Gaussian beam propagation equation

We performed a knife-edge measurement of the output laser beam from the tunable commercial QCL introduced above. The knife was mounted on a movable stage to displace its position in the z direction, while the movement in the xy plane was possible thanks to a THORLABS step motor allowing 5 μm steps. The laser beam was focused using a microscope objective with a focal length of 18 mm. The power was recorded by a THORLABS powermeter. The blade position has been scanned so to be sure to completely span the transient between the full power and the covered beam configurations. Without knowing a priori the focal position, we started placing the blade at the nominal distance of 18 mm from the objective. Then, we performed several measurements displacing the blade position along the z direction. In this way, we managed to observe the distance corresponding to the minimum value of the beam radius. For each measurement, the power derivative has been fitted using a Gaussian curve (Fig. 4.10(a)), from which we extracted the amplitude at the position corresponding to an intensity drop of a factor $1/e^2$ with respect to the maximum. The measured beam radii at each z are reported in Fig. 4.10(b): a divergence of the beam as we get far from the focus spot is clearly observable. The data are fitted using the equation for the Gaussian beam propagation:

$$w(z) = w_0\sqrt{1 + (\frac{z\lambda}{\pi w_0^2 n})^2} \tag{4.11}$$

with operating laser wavelength fixed at $\lambda \approx 9.2$ μm, $n = 1$, and the waist w_0 left as free fitting parameter. We thus obtained a laser beam radius at the focal spot of $w_0 = 0.0385$ mm, corresponding to a diameter of ≈ 77 μm. The same measurement is performed by scanning the knife position in the vertical - y - direction: the intensity distribution in this case is found to have a diameter measuring ≈ 69 μm. Thus, the ellipticity of the beam spot can be considered negligible, and the focusing area that will be necessary to calculate the intensity of the incident beam is obtained to be $A \approx 4,17\ 10^{-5}$ cm^2. Knowing that the numerical aperture (NA) of the objective lens is equal to 0.08, we can calculate the nominal focal spot size as

$$2r_{nominal} = 0.82\frac{\lambda}{NA} \tag{4.12}$$

The resulting radius is equal to $r_{nominal} \approx 47,1$ μm, corresponding to an area $A_{nominal} = 6.9\ 10^{-5} cm^2$, which is comparable with our result.

4.5 High intensity measurements

We can now move to the discussion of the results obtained for the high intensity measurements. Initially, the saturation measurement has been performed on sample HM4447. Again, we choose an array having a lateral size s that guaranteed us to work as close as possible to the anti-crossing point. The first step was a low intensity measurement aimed to replicate the reflectivity spectrum obtained with FTIR spectroscopy. Low intensity condition was ensured by setting the QCL current to its minimum operating value of 600 mA and the angle of the $\frac{\lambda}{2}$ plate to $\theta = 89°$. In this way we allow a small fraction of the radiation to pass. The laser wavelength was varied from 1016 cm^{-1} to 1320 cm^{-1} with steps of 4 cm^{-1}. Also in this case, we collected first the reference signal from a gold surface to obtain the normalized reflectance of the sample. Before every set of reference/sample acquisition, the polarizer in front of the MCT was adjusted to record a signal at maximum reflectance lying below 4 mV, in order to avoid the detector saturation. The result reported in Fig. 4.11(a) shows clearly the presence of two spectral minima corresponding to the upper and lower polaritons. After that, a high intensity measurement was finally taken. The maximum power delivery was ensured by removing the $\frac{\lambda}{2}$ plate - polarizer block and setting the QCL current to the maximum operating value of 1000 mA. Unfortunately, such a high power configuration limits the accessible wavelength range to 1040 cm^{-1} - 1140 cm^{-1}. Under high excitation intensity, the two polaritons collapse on a single dip as shown in Fig. 4.10(a), confirming the saturation of the intersubband transitions.

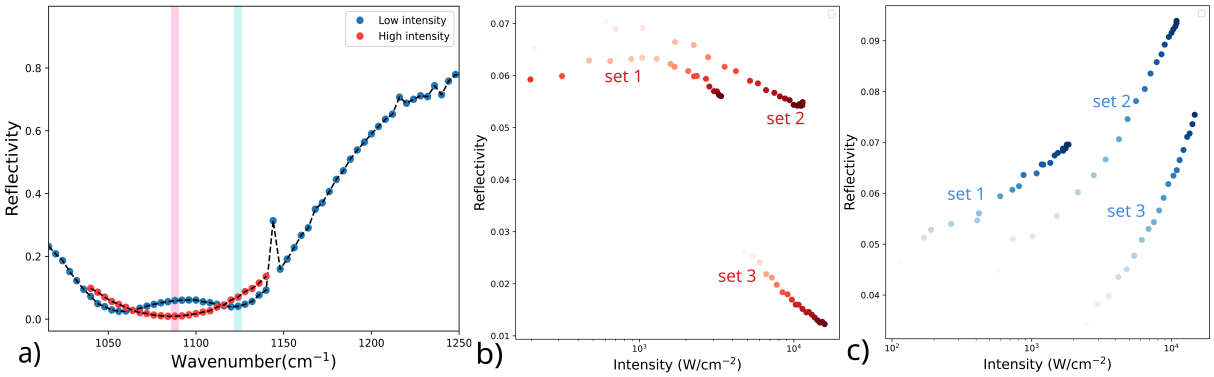

Figure 4.11: a) Low intensity (blue) and high intensity (red) reflectivity from HM4447. b),c) Reflectivity as a function of the excitation intensity at two different wavenumbers : 1124 cm^{-1} (c) and 1088 cm^{-1} (b)

The result is a decrease of the reflectance in the central part of the spectrum, whereas the reflectance is increased in correspondence of the two polaritons, making them suitable points to let the device operate as a SESAM. Once the saturation spectrum is obtained, we can study the non-linear reflectivity in correspondence of the different spectral features. For this purpose, we measured the variation of reflectivity as a function of the increasing excitation intensity in correspondence of both the upper polariton and the bistability point energies. To progressively increase the incident intensity at a fixed wavelength, we divided the measurement in three distinct sets, going from the minimum to the maximum incident intensity condition. First, the current was set to the minimum value of 600 mA varying the angle of the $\frac{\lambda}{2}$plate from 89° (fully closed condition) to 132° (fully open condition). Secondly, the same angle sweep was performed setting the value of the current to 1000 mA. Finally, to scan the power to its maximum value, we removed the $\frac{\lambda}{2}$plate - polarizer block and let the current vary from 600 mA to 1000 mA. These three sets of measurements were carried out recording two different signals: first, the sample response under increasing power was measured and normalized to the reference signal from the gold surface. After that, the sample was removed and a powermeter was placed after the objective to record the power delivered by the laser under the same conditions of the first measurement. What we obtain is thus a measurement of

the reflectivity as a function of the incident power. The result for HM4447 is reported in Fig. 4.11(b), (c). The two different plot display the variation of reflectivity in correspondence of the upper polariton (c), corresponding to the wavenumber ω=1124 cm^{-1}, and of the point in between the two polariton dips (b), corresponding to ω=1088 cm^{-1}. In both the cases, the trend in the reflectance is coherent with our expectation from the saturation spectrum: placing ourselves on the upper polariton position, as the incident intensity is increased we progressively move from the low intensity to the high intensity curve in Fig. 4.11(a), corresponding to an increasing reflectivity. The opposite is observed for ω=1088 cm^{-1}, where the reflectivity is decreased at high intensity. Unfortunately, as we can see from the figures, the data obtained from the three distinct sets of measurements going from low to high power do not stitch together. The reason for this is probably due to the removal and re-placing of the $\frac{\lambda}{2}$ plate - polarizer block switching from the sample to the powermeter measurement. This could in fact alter the measurement conditions between the measurements. This idea is even more reasonable if one looks at the data from each of the three set of measurements: while the two sets obtained before removing the optical block - and thus in the same conditions - show a slight discrepancy, this is clearly increased for the third measurement after the change of the element in the setup. Apart from this, the general trend observed in the reflectivity is coherent with the saturation spectrum.

	Wavenumber[cm^{-1}]	ΔR
LP	1056	2.2%
HP	1124	2.9%
Bistability	1088	-5.9%

Table 4.2: Wavenumbers of the three main spectral features and the respective variation of reflectance.

4.6 Effects of the funneling on the saturation intensity

Finally, we focus on the effect of funneling on the saturation intensity, by observing how this changes by varying the pitch p and so the density of microcavities in the array. We expect that increasing the distance between the patches, each of them will be able to harvest more photons thanks to the increasing effect of the effective collection area. The latter is in fact directly related to the filling factor, being inversely proportional to $(\frac{s}{s+p})^2$. As consequence, the single resonator injection is increased, boosting the saturation process. In this way, we aim to observe if the funneling effect can play a role in decreasing the value of the ISB saturation intensity. We performed a low and high intensity measurements, as the ones described in the previous sections, on arrays with pitch ranging from $p = 1$ μm to 7 μm from sample HM4448-A-2. For each of them, we choose again the array with a lateral size s ensuring two well balanced polaritons dips within the chip 2 wavelength range. The saturation measurement enabled us to check the position of the maximum variation in reflectance for each p. In every p we pumped in correspondence of the cavity absorption wavenumber, where the contrast between the two reflectivity spectra was maximum.

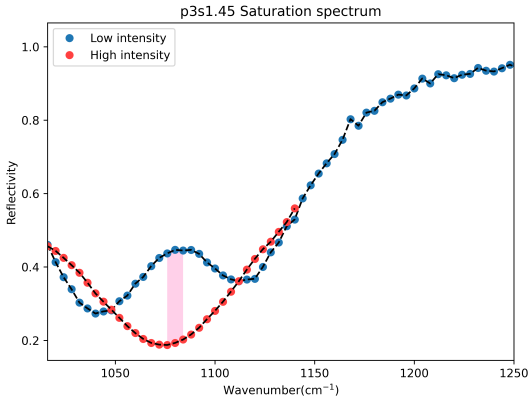

Figure 4.12: Saturation spectrum from HM4448-A-2 with $p = 3$ μm and $s = 1.45$ μm: the maximum variation of reflectance between the low intensity curve (blue) and the high intensity one (red) is found in between the two polaritons

The resulting saturation spectrum is reported in Fig. 4.12 for $p = 3$ μm and $s = 1.45$ μm. Again, we assist to the absorption saturation leading to the variation of reflectivity. Once the spectrum was measured, we fixed the wavenumber and we measured again the nonlinear optical response under an increasing incident power. The current setup is equipped with a couple of BaF_2 polarizers (one of them rotable) to avoid the problem of non-stitching data encountered before. Covering the entire MCT dynamic range, this allowed us to perform the power sweep on the sample and then on the powermeter in one single measurement for each instead of three. When the two BaF_2 polarizers are alligned, we assist to the largest transmission of power. As we start rotating the first polarizer with respect to fixed one, the power decreases with a 4^{th} power cosinusoidal behavior to a minimum transmittance when the two polarizers form an angle of 90°. Looking at the signal recorded by the powermeter, we noticed that approaching the orthogonal condition the value of the transmitted power was encountering the noise floor of the instrument. To exctract meaningful information about the signal at orthogonal angles of the polarizers, we fitted the data well above the noise floor. Through this procedure we were able to calibrate the instrument throughout the whole angle range (Fig. 4.13).

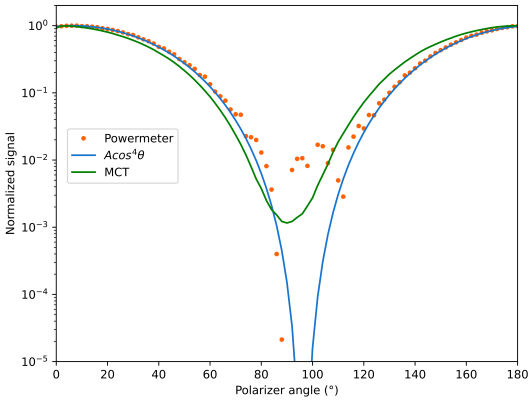

Figure 4.13: Plot of the recorded signal as a function of the angle between the two polarizers. The power measurement is affected by the instrument's noise floor as we approach low power condition (orange). The fitted curve used to extract values of the power is reported (blue). The green curve show how the MCT signal is recorded all over its dynamic, reproducing the 4^{th} power cosinusoidal.

As we can see from the figure, orange dots represent the power measured by the powermeter: as we approach the polarizer orientation $\theta \approx 90°$ the signal starts being strongly affected by the instrument noise level. On the contrary, by properly fitting the data (blue curve), we can access the power delivered through the two polarizers when they are oriented almost orthogonally. We can now move to the discussion of the results obtained measuring the saturation intensity as function of the pitch size. Every power scan has been carried out feeding the QCL with the maximum current of 1000 mA, while the polarizer angle was varied from 0° to 100°. Again, when measuring the sample reflectance, a polarizer is placed in front of the MCT and adjusted to leave the maximal response below the saturation threshold of 4 mV. Once both the normalized signal and the power are measured, we finally plot the saturable absorber reflectivity as a function of the incident intensity.

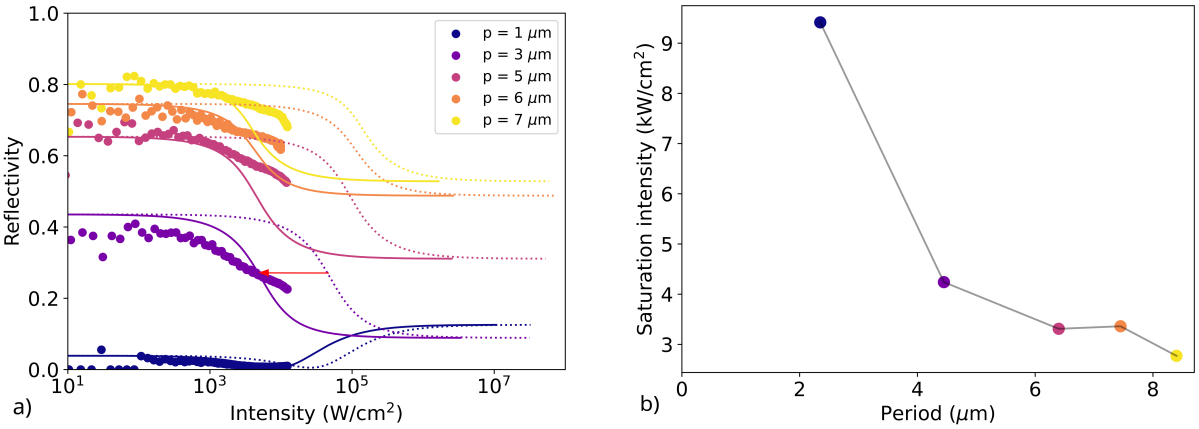

Figure 4.14: a) Experimental result of the reflectivity as function of the intensity (dotted) and the CMT fitting curves. b) Values of I_{sat} extracted by the CMT fitting curves and plotted as a function of p

For each value of p, the reflectivity curve is fitted by using the respective expression from Coupled Mode Theory, as reported in Fig. 4.14(a). Here, for each reflectivity curve the fitting is performed both with (continuous lines) and without (dashed lines) taking into account the filling factor term in the formula

from CMT. As indicated, when the filling factor is taken into account we have a shift of the nonlinear curve with saturation towards lower intensities. Moreover, we can notice how the shift magnitude becomes more relevant as we increase the value of the pitch p. This is already a first indication on the effect of a smaller filling factor in reducing I_{sat}. Now we can use the CMT fitting curves to access values of the saturation intensity I_{sat} at which the population of the upper subband is equal to $n_2 = n_s/4$. The dependence of I_{sat} on the pitch is thus found and reported in Fig. 4.14(b): the smaller the density of cavities in the array, the smaller the intensity needed to saturate the intersubband absorption. These results give important information on the role played by the funneling in the saturation of microcavity array's absorption. Reducing the filling factor of the array, and thus increasing p, the fraction of the total incident intensity contributing to the absorption is smaller, as seen in Fig. 4.6. At the same time, increasing the space between the resonators, the funneling effect becomes more efficient, allowing them to effectively "capture" the incident field lines from a larger area. This clearly helps to boost and finally saturate the ISB transition. The decrease of the saturation intensity thus witnesses that the increase of the photon harvesting efficiency is such to counteract the progressive departure from the critical coupling condition. This constitute an additional step in the development of a SESAM working in the mid-IR with a sustainable saturation intensity.

Chapter 5

Future perspectives

5.1 Ultrafast SESAMs characterization

An important step in the further development of mid-IR saturable absorber mirrors will be an accurate analysis of the absorption saturation dynamics. This will be possible by means of degenerate ultrafast pump-probe spectroscopy: a probe constantly monitors the reflectance signal from the sample, while a high intensity pump pulse saturates the ISB transitions. The key is to shape narrow pump and probe pulses both centered on one of the polariton spectral features. In this way, thanks to the presence of the probe, we are able to observe the time evolution of the polariton state populations, and thus of the ultra fast saturation.

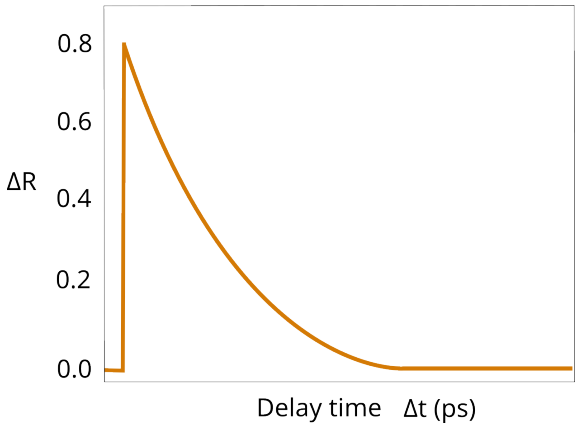

Figure 5.1: Sketch of the time evolution of the reflectance in correspondence of the polariton: the reflectivity varies as function of the delay time with respect to the pump pulse. At $\Delta t = 0$, the ISB transitions are saturated and the reflectance pops up. As time delay increases, the probe monitors a recover of the polaritons.

5.2 Stimulated Polariton-Polariton scattering in dispersive microcavities

The bosonic character of the intersubband polaritons constitutes another very attractive topic to explore. Unlike this work, the bosonic properties we want to investigate are observed in dispersive cavities. Important results could be obtained relying on ultrafast pump-probe experiments. In this case we need non-collinear pulses with an ultrabroadband probe monitoring the time evolution of the whole spectrum. By pumping at the inflection point of the lower polariton branch, we are able to activate a stimulated polariton-polariton scattering process (Fig. 5.2(b)). Here, the polariton scattering rate toward the lowest energy state is proportional to the population of the state itself.

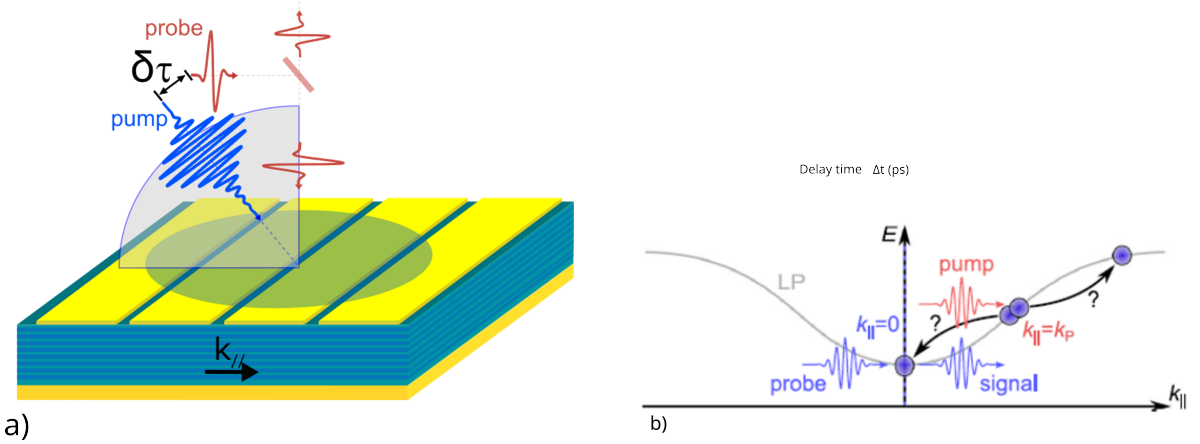

Figure 5.2: a) Scheme of the noncollinear pump-probe spectroscopy. The delay time between the two pulses is indicated. b) Scheme of the stimulated polariton-polariton scattering. The latter is observed by pumping at the inflection point of the lower polariton branch and in presence of a probe pulse at the energy minimum in correspondence of $k_{//}=0$

This bosononic effect takes the name of *final state stimulation*. Thanks to it, increase of the signal in correspondence of the lower polariton it is observed. The aim is to start from this process to study the ultrafast bosonic properties of the system and to move the first step toward the first demonstration of an inversionless lasing system based on intersubband polaritons.

Bibliography

[1] Julien et al. “Optical saturation of intersubband absorption in GaAs-Al/GaAs quantum wells”. In: *Applied Physics Letters* 53.2 (1988), pp. 116–118.

[2] Dini et al. “Microcavity Polariton Splitting of Intersubband Transitions”. In: *Physical Review Letters* 90.11 (2003), p. 116401.

[3] Keller. “Recent developments in compact ultrafast lasers”. In: *Nature* 424.6950 (2003), pp. 831–838.

[4] Lockyear et. al. “Thin resonant structures for angle and polarization independent microwave absorption”. In: *Applied Physics Letters* 94.4 (2009), p. 041913.

[5] Todorov et al. “Strong Light-Matter Coupling in Subwavelength Metal-Dielectric Microcavities at Terahertz Frequencies”. In: *Physical Review Letters* 102.18 (2009), p. 186402.

[6] Todorov et al. “Optical properties of metal-dielectric-metal microcavities in the THz frequency range”. In: *Optics Express* 18.13 (2010), p. 13886.

[7] Pardo et. al. “Light Funneling Mechanism Explained by Magnetoelectric Interference”. In: *Physical Review Letters* 107.9 (2011), p. 093902.

[8] Todorov et al. “Intersubband polaritons in the electrical dipole gauge”. In: *Physical Review B* 85.4 (2012), p. 045304.

[9] Todorov et al. “Polaritonic spectroscopy of intersubband transitions”. In: *Physical Review B* 86.12 (2012), p. 125314.

[10] Zanotto et al. “Ultrafast optical bleaching of intersubband cavity polaritons”. In: *Physical Review B* 86.20 (2012), p. 201302.

[11] Todorov et. al Chen. “Microcavity Enhanced Quantum Well Infrared Photodetector”. In: *Optica Publishing Group* CLEO: $QELS_{F}undamentalScience$.3 (2013).

[12] Feuillet et. al Todorov. “Strong near field enhancement in THz nano-antenna arrays”. In: *Scientific Reports* 3.1 (2013), p. 1361.

[13] Manceau et. al. “Mid-infrared intersubband polaritons in dispersive metal-insulator-metal resonators”. In: *Applied Physics Letters* 105.8 (2014), p. 081105.

[14] Zanotto et al. “Perfect energy-feeding into strongly coupled systems and interferometric control of polariton absorption”. In: *Nature Physics* 10.11 (2014), pp. 830–834.

[15] Todorov et. al Nga. “Antenna-coupled microcavities for enhanced infrared photo-detection”. In: *Applied Physics Letters* 104.3 (2014), p. 031113.

[16] Bruno Paulillo. “Circuit-tunable subwavelength terahertz devices”. In: *Theses* Universitité Paris Saclay (COmUE), June 2016. (2016).

[17] Orlov et al. “Toward a Corrected Knife-Edge-Based Reconstruction of Tightly Focused Higher Order Beams”. In: *Frontiers in Physics* 8 (2020). DOI: `https://doi.org/10.3389/fphy.2020.527734`.

[18] Jeannin et al. “Unified description of saturation and bistability of intersubband transitions in the weak and strong light-matter coupling regimes”. In: *Physical Review Letters* 127.18 (2021), p. 187401.

[19] Qin et al. “Semiconductor saturable absorber mirror in the 3–5 µm mid-infrared region”. In: *Optics Letters* 47.4 (2022), p. 890.

[20] Knorr et. al Manceau. “Intersubband Polariton-Polariton Scattering in a Dispersive Microcavity”. In: *Physical Review Letters* 128.24 (2022), p. 247401.